Active control of swept shock wave/turbulent boundary-layer interactions

J. S. Couldrick, S. L. Gai, J. F. Milthorpe and K. Shankar
School of Aerospace & Mechanical Engineering, University College
Australian Defence Force Academy, Canberra, Australia

ABSTRACT

This paper looks at active control of the swept shock wave/turbulent boundary-layer interaction using smart flap actuators. The actuators are manufactured by bonding piezoelectric material to an inert substrate to control the bleed/suction rate through a plenum chamber. The cavity provides communication of signals across the shock, allowing rapid thickening of the boundary-layer approaching the shock, which splits into a series of weaker shocks forming a lambda shock foot, reducing wave drag. Active control allows optimum control of the interaction, as it would be capable of positioning the control region around the original shock position and control the rate of mass transfer.

The actuators are modelled using classical composite material mechanics theory, namely analysis of a laminate with a uniform cross section. Furthermore a finite element modelling program (ANSYS 5.7) was used to produce improved results.

NOMENCLATURE

A	extensional stiffness matrix
B	coupling stiffness matrix
$C_{\mathbf{d}}$'	point drag coefficient
$C_{\mathbf{d}}$	drag coefficient
d_{31}	piezoelectric charge constant
D	bending stiffness matrix
E	Young's modulus
I	second moment of area
l	test section length
L	streamline
M	moment
M_n	normal Mach number
N	load
P	pressure
S	shock position
t	thickness
V	applied voltage
x	distance along surface
X	normalised substrate thickness
Z	normalised substrate Young's modulus
β	shock angle
δ	unimorph deflection
Δ	difference in shock angles ($\beta_{fs} - \beta_s$)
κ	curvature
ν	Poisson ration
θ	leading shock angle

Superscript

o	mid plane

Subscripts

i	induced
fs	front shock
0	stagnation
P	piezoceramic properties
s	main shock
S	substrate properties
t	test section
1	freestream (upstream of wedge shock)
V	applied voltage
W	pressure load

Abbreviations

ACSBLI	active control of SBLI
EDM	electro discharge machining
FEM	finite element modelling
PCSBLI	passive control of SBLI
PZT	lead zirconate titanate
SBLI	shock wave/boundary-layer interaction

Paper No. 2821. Manuscript received 3 January 2003, revised version received 9 May 2003, accepted 6 June 2003.

https://doi.org/10.1017/S0001924000005042 Published online by Cambridge University Press

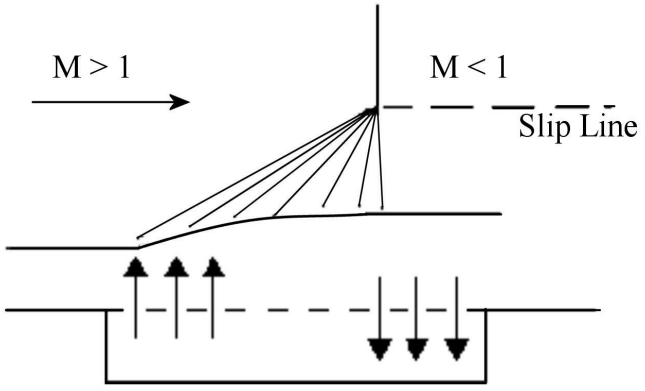


Figure 1. Passive control of the shock wave/boundary-layer interaction (PCSBLI).

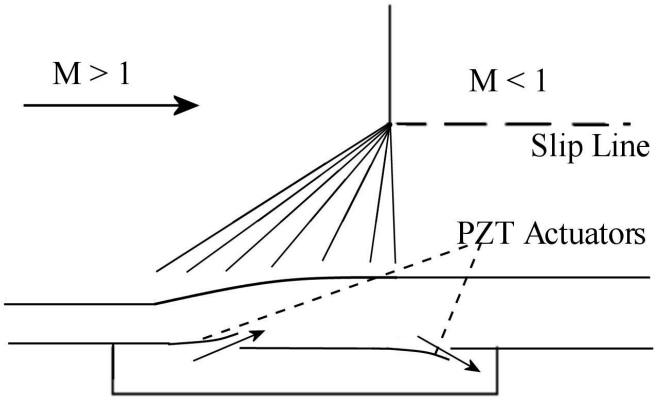


Figure 2. Active control of the shock wave/boundary-layer interaction (ACSBLI).

1.0 INTRODUCTION

For very weak shock waves, with an upstream Mach number of around 1·1, the extent of the shock wave/boundary-layer interaction is relatively weak, allowing the normal shock wave to extend into the boundary-layer virtually as far as the sonic line with little smearing[2,3]. However, as the upstream Mach number increases, the distortion of the shock foot due to boundary-layer thickening becomes increasingly significant. Above an upstream Mach number of around 1·3 incipient separation occurs and the shock wave foot bifurcates above the boundary-layer to form a lambda (λ) foot[4-7]. The leading shock is usually highly oblique with the trailing part of the lambda foot nearly normal.

Previous work[8-17] has been to passively control the interaction by replacing the surface beneath the foot of the shock wave with a porous plate covering a plenum chamber, (Fig. 1). This allows high-pressure air from the flow downstream of the shock wave to re-circulate through the plenum chamber into the low-pressure flow upstream of the wave. The cavity provides communication of signals across the shock, allowing rapid thickening of the boundary-layer approaching the shock, which splits into a series of weaker shocks forming a lambda shock foot, reducing wave drag. Furthermore, the suction down-stream reduces separation and viscous losses.

Historically, active control of shock/boundary-layer interaction (ACSBLI) has been hampered by the drag reduction

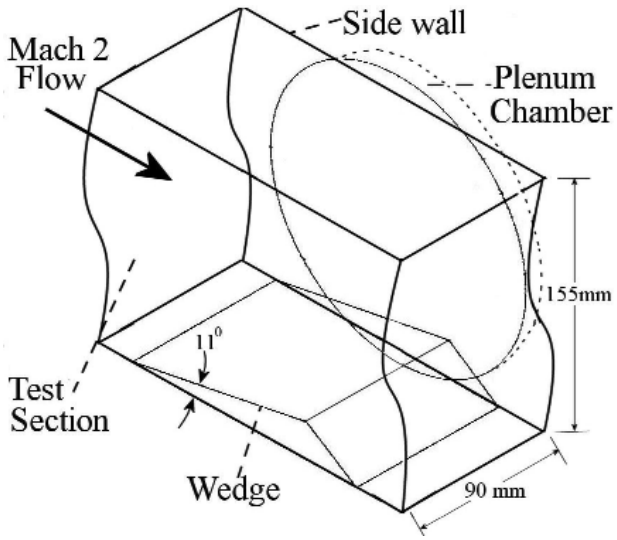


Figure 3(a). Wedge flush to the tunnel floor and shown in relation to the test section.

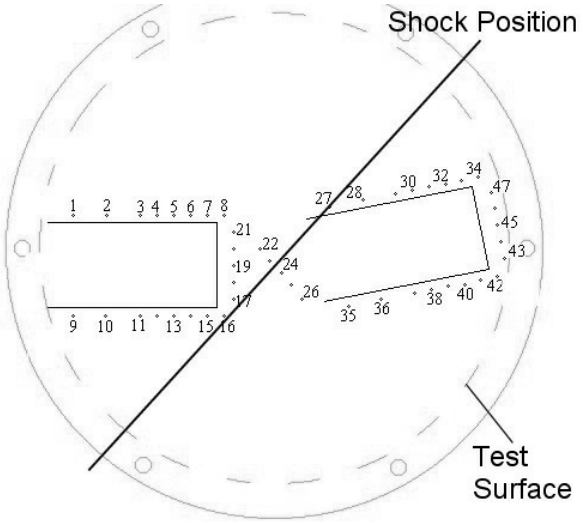


Figure 3(b). pressure port layout on test surface.

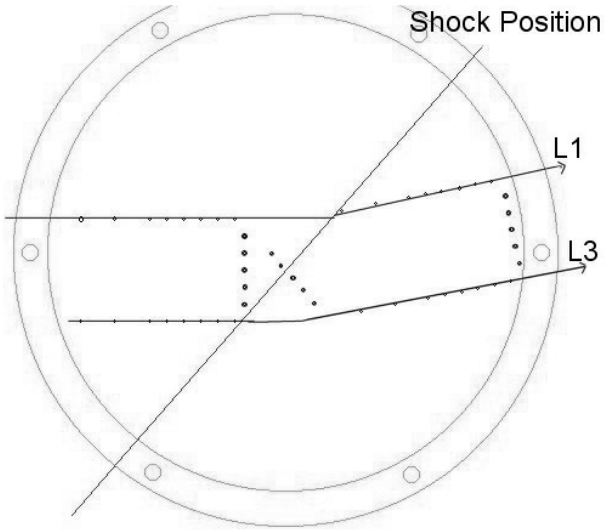


Figure 3(c). measurement co-ordinate system.

https://doi.org/10.1017/S0001924000005042 Published online by Cambridge University Press

achieved being negated by the additional drag due to the power requirements, for example, the pump in the case of mass transfer and the drag of the devices in the case of vortex generators. The object of the present research[18-20] is to assess the concept of active control using 'smart' flap actuators, (Fig. 2). The actuators are designed using PZT-5H piezoelectric material to control bleed/suction rate.

The plenum chamber pressure would approximately be at a mean pressure of the upstream and downstream pressure. Using this assumption, the pressure difference acting on the actuator will, therefore, be the difference between the chamber pressure and the free stream pressure.

As active control should be capable of positioning the control region around the original shock position and hence control the rate of mass transfer, a number of design options were considered for the integration of the PZT into the structure. These included the use of unimorph actuators with the PZT attached to one side of an inert substrate, bimorph actuators with two opposite poled PZT layers attached to each other to create twice the moment and also polymorphs with numerous PZT layers to further improve deflection characteristics. In addition, both bimorphs and polymorphs can be directly employed as actuators. However, the present paper describes actuators of the unimorph variety.

2.0 EXPERIMENTAL ARRANGEMENT

The work was carried out in a blow-down supersonic wind tunnel and a swept shock interaction was produced on the tunnel side wall, giving a normal shock Mach number (M_n) of 1·3 with a wedge of 11° mounted on the floor in a Mach 2·0 free stream, (Fig. 3(a)). For a static pressure in the test section of 44kPa the smart flaps will then have a 17·64kPa pressure difference acting across them.

A plenum chamber (140mm × 20mm) is placed underneath the swept shock in the sidewall of the test section. This is covered by a plate containing the 'flaps' and numerous pressure ports, (Fig. 3(b)). The flaps were cut into the plate, by electro discharge machining (EDM), with a gap of 0·05mm between the model skin and the flap. The piezo-ceramic is bonded to the underside of the flap and a voltage is applied to control the actuator deflection and thus mass transfer rate. The surface pressures were recorded using a single transducer which steps through the various ports using a scanivalve. Surface pressures were recorded in both streamwise and transverse directions, as shown in Fig. 3(c).

3.0 STRUCTURAL ASPECTS OF THE UNIMORPH ACTUATOR

3.1 Configuration

The concept for the unimorph set-up was to have the piezoceramic embedded within the surface material, (Fig. 4), to allow a greater bonding area and improved deflection properties, while retaining a flush upper surface. A lip was then incorporated into the design to minimise the deflection required before mass transfer occurred.

The tip deflection varies with the substrates' Young's Modulus and thickness. The selection of substrate is a trade-off between suppressing the deflection due to the pressure difference across the flap, while keeping the unimorph electrically flexible to create active control. Active control of the shock boundary-layer interaction requires that the flaps are able to close and have zero deflection, minimum mass transfer, to be regarded as capable of active control. This trade-off restricts the substrate to a Young's Modulus similar to that of the piezoceramic, giving aluminium as a suitable substrate material. It was hoped to achieve better piezoelectric performance in testing than theory suggests due to the assumption of a constant mean pressure within the plenum chamber. In reality, there will be a pressure gradient in the plenum and spillage around the side edges, which will reduce the pressure acting on the flaps.

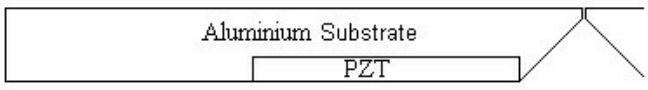


Figure 4. Modified unimorph flap configuration.

3.2 Theory

Classical theory uses composite material mechanics theory, namely analysis of a laminate with a uniform cross section. It assumes an infinitely strong bond between the piezoceramic and substrate and also a constant pressure load acting across the entire unimorph area. It assumes that the total uniform deflection is a summation of the pressure and piezoelectric deflection.

3.2.1 Unimorph tip deflection for an applied voltage (δ_V)

Using piezoelectric and laminate theory the deflection obtained when a piezoceramic is attached to an inert substrate is given by,

$$\delta_V = \frac{k_i}{2} * L^2 \qquad \ldots (1)$$

$$\begin{Bmatrix} \in_i^o \\ \kappa_i \end{Bmatrix} = \begin{bmatrix} \mathbf{A}_i & \mathbf{B}_i \\ \mathbf{B}_i & \mathbf{D}_i \end{bmatrix}^{-1} \begin{Bmatrix} N_i \\ M_i \end{Bmatrix} \qquad \ldots (2)$$

From Equation (2) it can be seen that the extensional stiffness matrix, $\mathbf{A_i}$, relates the induced mid-plane strains, $\in^o_i$, to the induced in-plane forces, N_i, and the bending stiffness matrix, $\mathbf{D_i}$, relates the curvatures, κ_i, to the induced moments, M_i. The coupling stiffness matrix, $\mathbf{B_i}$, couples the induced mid-plane strains, $\in^o_i$, to the induced moments, M_i, and the curvatures, κ_i, to the induced in-plane forces, N_i.

The in-plane forces, N, and moments, M, are induced by the piezoelectric characteristics and can be calculated using,

$$N_{xi} = N_{yi} = \frac{\mathrm{E_P} d_{31}}{(1-\nu_P)} * V \qquad \ldots (3)$$

$$M_{xi} = M_{yi} = -\frac{\mathrm{E_P} d_{31} t_s}{2(1-\nu_P)} * V \qquad \ldots (4)$$

3.2.2 Unimorph deflection for a given pressure load (δ_W)

Similarly laminate theory predicts the unimorph deflection under a given load as,

$$\delta_W = P*b*L^4/(8*(EI)_{eff}) \qquad \ldots (5)$$

https://doi.org/10.1017/S0001924000005042 Published online by Cambridge University Press

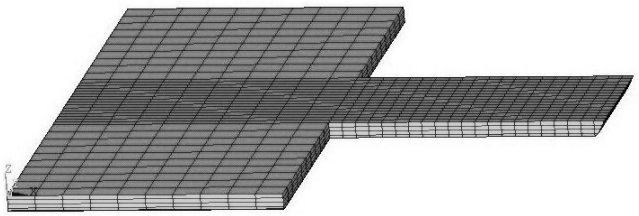


Figure 5. Unimorph finite element model in ANSYS 5.7.

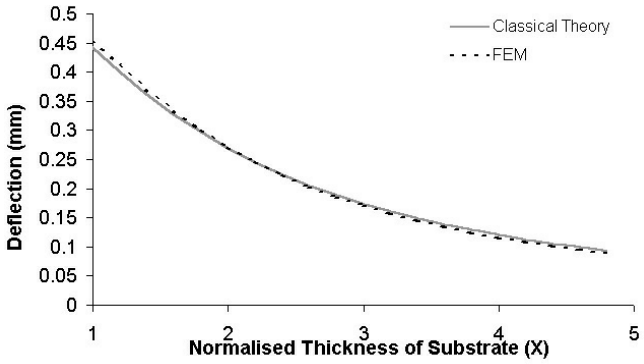


Figure 6. Unimorph deflection *vs* normalised substrate thickness for 500V.

where

$$\begin{Bmatrix} \epsilon^o \\ \kappa \end{Bmatrix} = \begin{bmatrix} \mathbf{A} & \mathbf{B} \\ \mathbf{B} & \mathbf{D} \end{bmatrix}^{-1} \begin{Bmatrix} N \\ M \end{Bmatrix} \quad \ldots (6)$$

$$(EI)_{eff} = b / d_{11} \quad \ldots (7)$$

3.3 Finite element modelling

ANSYS 5.7 was utilised as the FEM program with a parametric design language program modelling the unimorph flap as well as the supporting structure. Furthermore, it allowed modelling of the solid substrate tip and analysis of complex pressure loadings, which satisfy aerodynamic boundary conditions. In contrast, the classical theory is only approximately valid to simple approximate loads.

The model consists of 3,144 Solid95 Brick elements with 1,344 elements to model the unimorph, (Fig. 5). This grid resolution was chosen as a balance between computational cost and sufficient accuracy. Zero deflection boundary conditions were placed on all edges of the supporting structure allowing the unimorph flap to freely deflect.

3.4 FEM *vs* Classical theory — zero load

Both modelling systems were applied to compare and observe piezoelectric deflections for varying substrate Young's modulus and thickness. This unimorph design optimisation creates maximum deflection characteristics, while retaining the ability to 'close' the flap and have zero deflection.

The substrate's thickness and Young's modulus were normalised to the unimorph's thickness and Young's modulus in Figs 6 and 7. The predicted deflection is the result of a 500V applied field to the piezoceramic.

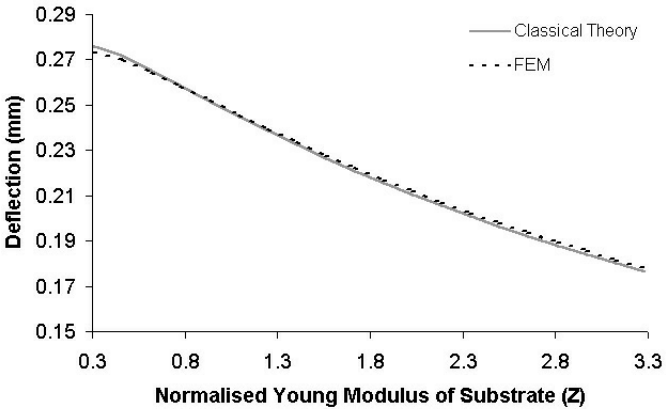


Figure 7. Unimorph deflection *vs* normalised Young's modulus for 500V.

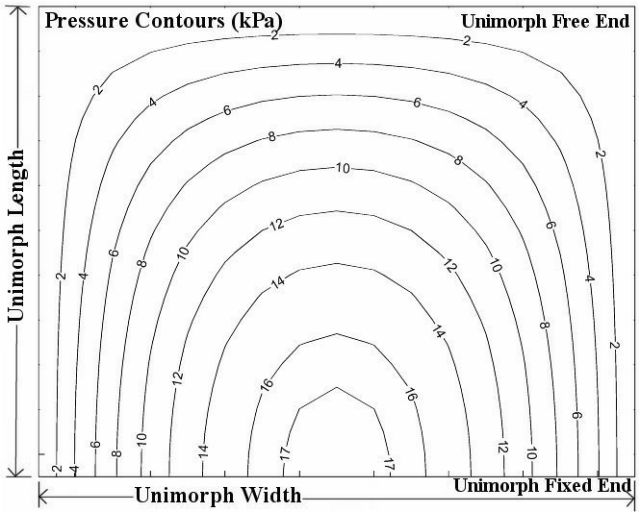


Figure 8. Quadratic pressure load map with isobars.

Figure 6 shows a reduction in deflection for an increase in the substrate thickness. This is expected as this implies an increase in the overall unimorph (beam) thickness and second moment of area of the beam ($I \approx t^3$), where tip deflection is inversely proportional to I. The tip deflection shown varies to approximately an inverse of the thickness.

Figure 7 shows an almost linear correlation between tip deflection and Young's Modulus ratio. This is expected as the Young's Modulus effects tip deflection directly.

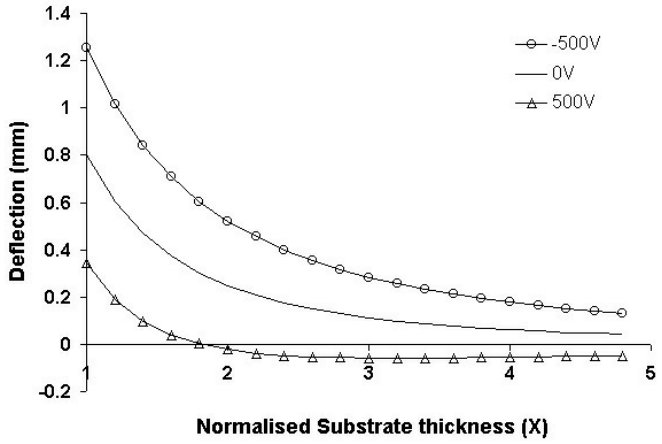
For both Figs 6 and 7, the two modelling theories show very good correlation with each other, varying by less than 1%.

3.5 FEM *vs* classical theory — working load

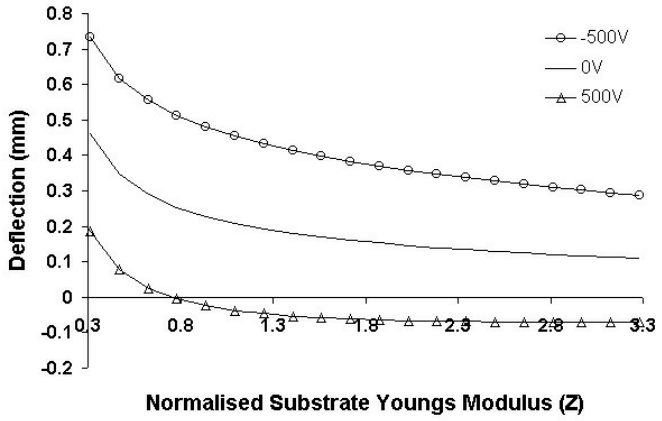
The main advantage of FEM is that complex pressure loadings can be applied that satisfy boundary conditions. The basic boundary condition is that there is no pressure load at the flap edges. A parabolic load distribution was applied (Fig. 8).

A maximum pressure, 17·64kPa, is used which is equivalent to half the difference of the pressure rise over the shock. The pressure drops off to zero at the flap edges producing a more realistic loading and deflection predictions (Figs 9(a) and 9(b)). The quadratic pressure loading gives the following deflection characteristics.

https://doi.org/10.1017/S0001924000005042 Published online by Cambridge University Press



(a)



(b)

Figure 9. FEM tip deflection predictions for a quadratic load and a 500V applied field while varying substrate (a) thickness (b) Young's modulus.

Figures 9(a) and (b) show that as the substrate thickness and Young's Modulus are increased, the tip deflection decreases, approximately inversely to the ratios. This is to be expected as the thicker and stiffer the substrate, the more constrained the unimorph will be.

If the unimorph has to be capable of zero deflection to provide active control then for a 500V limit the substrate has to be at least 0·9mm thick ($X = 1{\cdot}8$) for a 70GPa Young's modulus or 50GPa ($Z = 0{\cdot}78$) for a 1.1mm thickness.

The final unimorph design used a substrate thickness and Young's modulus of 1·1mm and 70GPa, respectively. These values give 0·5mm maximum tip deflection, ensure closure and the flap can be manufactured relatively flat.

4.0 RESULTS AND DISCUSSION

4.1 Oil flow visualisation

Tests were conducted on the interaction region using oil flow visualisations (Fig. 10). A water-soluble pen was used to trace and enhance the surface streamlines, allowing the surface flow features to be recorded using a digital camera.

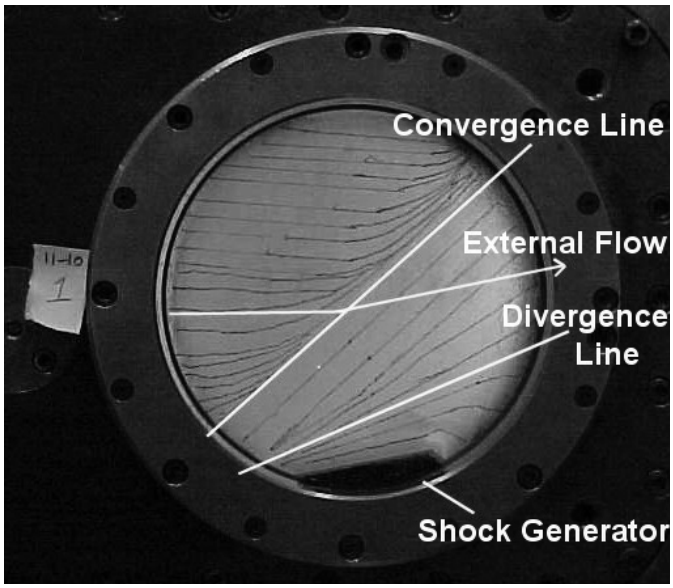


Figure 10. Pen enhanced oil flow visualisation without control.

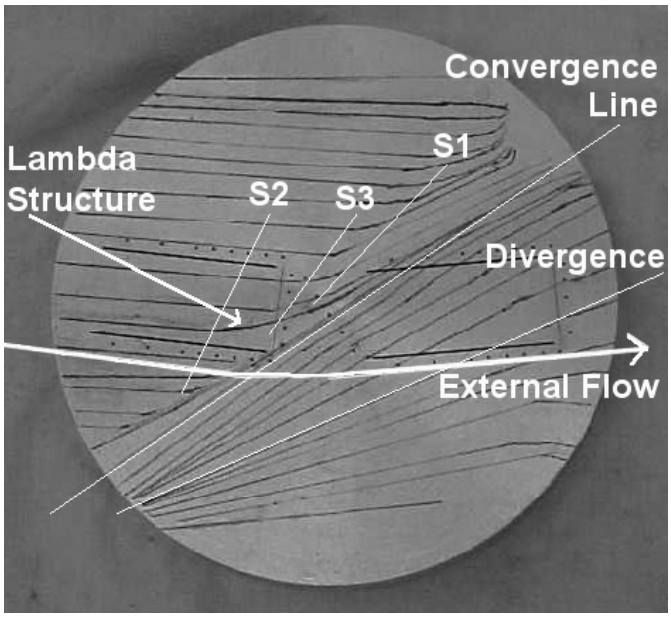


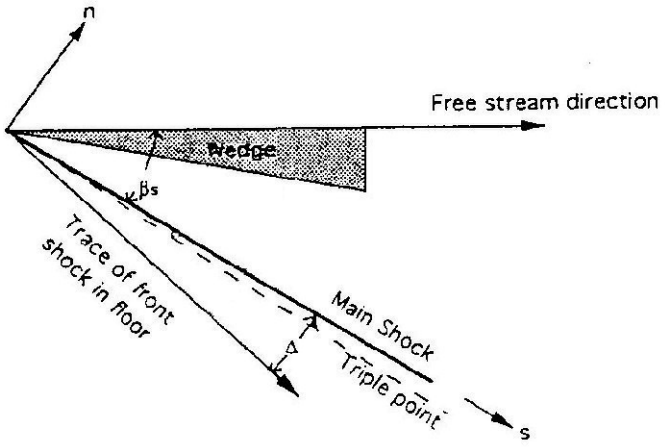
Figure 11. Pen enhanced oil flow visualisation with control.

Referring to Fig. 10, the flow is from left to right, with the wedge shock parallel to the convergence line. It can be seen that the shock is at approximately 41°, with an inviscid flow deflection angle of 11°.

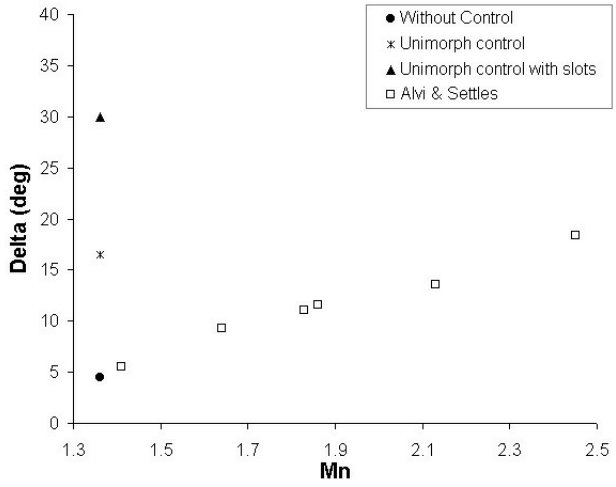
With the 11° wedge and a shock normal Mach number of 1·3 the flow would be separated incipiently according to Korkegi's criterion[7]. Also, according to Kubota and Stollery[5], for a freestream Mach number of 2, incipient separation occurs for a wedge angle between 10° and 12° so that the present flow is on the verge of separation. Figure 10 indicates that this is, indeed, the case as verified by the fact that the surface streamlines upstream of the shock converge to become parallel to the wedge shock.

Figure 11 shows the flow features with control. It can be concluded, from the parallel streamlines down stream of the convergence line, that the flow is incipiently separated. Furthermore, the divergence (shock generator reattachment) line can be observed,

https://doi.org/10.1017/S0001924000005042 Published online by Cambridge University Press



(a)



(b)

Figure 12(a). Co-ordinate system and (b) Variation of Δ [=(β_{fs}– β_s)] for front shock with normal Mach number (after Squire[21]).

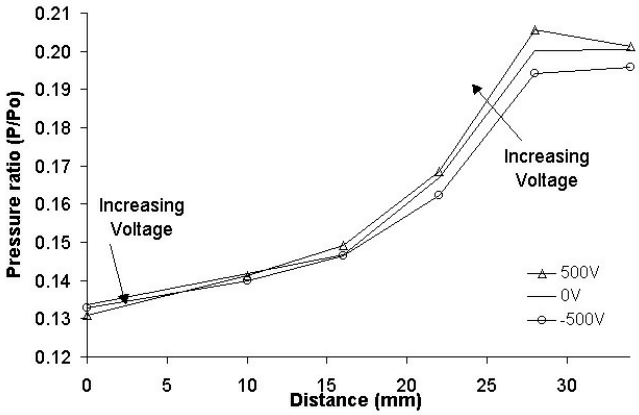


Figure 13. Surface pressure distribution along the normal to the wedge shock.

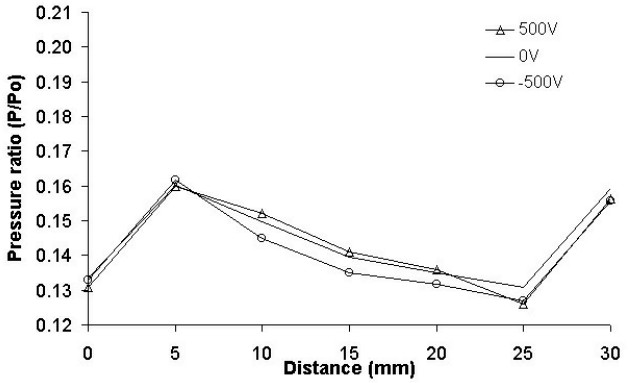


Figure 14. Surface pressure distribution along the front edge of the upstream unimorph.

which is a characteristic of re-attaching flow. There is a corner vortex generated by flow separating from the wedge and re-attaching to the sidewall creating the divergence line. The S1, S2, and S3 lines indicate separation lines: without control; with flap control; and with flap and slot control respectively. S2 and S3 are confirmed from pressure distribution readings. The wedge shock, as shown in Fig. 10, is found to occur at approximately the same angle and position as the convergence line and has been omitted from the above figure for reasons of over crowding.

The main shock generated by the wedge will occur parallel with the convergence line and has an angle, bs, of 41° to the horizontal, agreeing with Fig. 10. The S1 shock is the leading edge of the lambda foot, without control, and indicates the initiation of separation. The S1 angle, β_{fs}, is 45·5°, which gives a Δ [= (β_{fs}– β_s)] of 4·5°. This agrees with the trend of Alvi and Settles[3] work of swept interaction without control , as shown in Fig. 12(b), according to Squire[21].

The S2 and S3 shock angles indicate the leading-edge shock at the start of the interaction control. These are shock angles, β_{fs}, of 57·5° and 71° respectively, which relate to Δ of 16·5° and 30° respectively (Fig.12). These signify leading shocks that are anchored further away from the main shock, indicating a weaker front shock and consequent reduction in wave drag.

4.2 Surface pressures

The surface pressure ratios were recorded for actuator control, at various actuator deflections (applied voltage), normal to the original shock position and along the end of the upstream unimorph, (Figs 13 and 14).

Figure 13 shows the pressure rise normal to the original shock, from pressure port 8 (x = 0mm) through to 26 (x = 34mm) (Fig. 3(b)), up to the plateau as observed by Babinsky[16]. The rise is gradual compared to the pressure rise across an inviscid shock. Increasing the voltage (i.e. reducing unimorph deflection) reduces the upstream pressure by decreasing the mass transfer from the higher pressure plenum. It also has the effect of increasing the plateau pressure, which suggests a decrease in the reduction in drag, that is reduced deflection gives less control and higher drag coefficients.

Figure 14 shows the pressure rise along the end of the upstream unimorph, from pressure port 8 (x = 0mm) through to 16 (x = 30mm) (Fig. 3(b)). A maximum and minimum can be observed, due to the rise in pressure across the shock and the thickening of the boundary-layer due to the mass injection respectively. The pressure rises at the end as the overall pressure has to rise across the shock.

The surface pressure ratios were recorded for actuator control at various actuator deflections (applied voltages) along L1 and L3. Distances are shown from the calculated wedge shock position (Fig. 3(c)) with a negative distance implying upstream. These were

https://doi.org/10.1017/S0001924000005042 Published online by Cambridge University Press

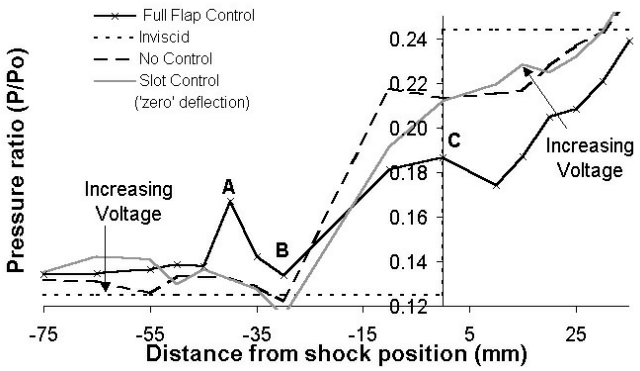


Figure 15. Surface pressures along L1.

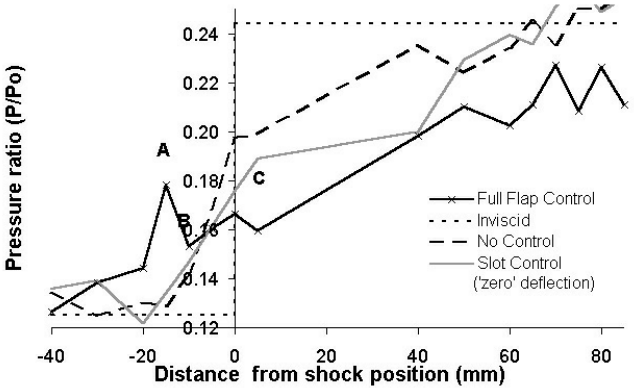


Figure 16. Surface pressures along L3.

compared with the inviscid pressure rise with no control, shown as a dashed line in Figs 15 and 16.

Figure 15 shows the pressure distribution for shock wave/boundary-layer interaction control with: flap control using 'Smart' flaps with the trend shown for increasing voltage; theoretical inviscid pressure rise; no control and slot control to indicate zero flap deflection.

The pressure rise without control can be seen, from the graphs, to agree closely with Babinsky[16]. Initial pressures rise due to front shock of the bifurcated lambda-shock structure followed by plateau region and then rise towards inviscid value.

The pressure rise with flap control along L1 shows: a local pressure maximum (A) which indicates the leading edge shock position; a local pressure minimum (B) that is a result of expansion waves and boundary-layer thickening; and a pressure plateau (C). This is similar to the results of Babinsky's[16] active control with slots, both in shape and magnitude. These attributes indicate that the shock wave separates to form a lambda-like structure thereby suggesting a spreading of the shock foot and result in a reduction in wave drag.

Also, the pressure ratios before the plateau are reduced with increased voltage, reduced unimorph deflection. Increased unimorph deflection leads to greater mass transfer from the higher plenum pressure in the chamber. This is reversed for downstream pressure ratios where increased mass transfer bleeds off the higher pressures to the lower pressures in the plenum chamber. The initial upstream pressure ratio recorded does not reach the inviscid value as a result of interaction due to flow escaping through the gaps between the model skin and the flap upstream of the first pressure port.

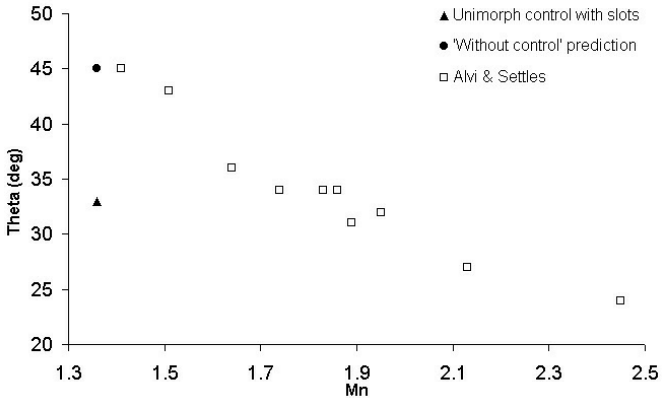


Figure 17. Variation of θ with normal Mach number (after Squire[21]).

It can be seen that the pressure ratio without control, compared to flap control, is greater at the start of the control region due to the bleed mass transfer injecting higher-pressure flow into the boundary-layer. After the end of the upstream flap the control pressure ratio reduces to less than that without control. Furthermore, the plateau with flap control is at approximately half the pressure rise across the main shock whereas, without control, the plateau is located at the 70% value of the total pressure rise, suggesting an extended region of interaction.

The slot control pressure rise agrees closely to the no control pressure rise, indicating that the interaction control has been greatly reduced. However, the pressure rise is more gradual with a less prominent plateau compared to without control, which can be attributed to interaction control from the slots.

Figure 16, showing the pressure rise along L3, allows the interaction to be observed for an increased downstream control region and has similar characteristics to Fig. 13. The local maximum (A) is greater because the leading edge shock is closer to the original shock position. This presents a more normal shock to the flow and therefore an increased pressure rise. The local minimum (B) is again greater than for L1; however, it is uncertain whether the magnitude of difference between maximum and minimum is less along L3 due to closer proximity to the maximum, plateau (C) or that the boundary-layer has not thickened to the same degree. For similar reasons it is uncertain why the plateau is at a lower pressure than the local maximum. The pressure fluctuations downstream are assumed to be due to the local interaction with the trailing edge of the lambda structure and the thinning of the boundary-layer.

Figures 15 and 16 show the final pressure ratios are less than the inviscid value. The final downstream pressure ports are just outside of the interaction region and it is expected than they are still being influenced by the interaction control.

It is assumed that with a 500V applied electric field to the piezoceramic, zero deflection of the unimorph results. However, interaction characteristics are still observed due to mass transfer through the gaps between the model skin and the flap. Furthermore, zero deflection is only an assumption, as precise deflection measurement devices are unavailable at present.

From Figs 15 and 16 the pressure ratios across the front shock can be calculated as the pressure ratio of the local maximum divided by the pressure ratio of the port upstream of the local maximum. In both cases the pressure ratio across the shock is approximsately 1·22 (M_n = 1·09), which equates to a leading shock angle, θ, of 33°. This is an improvement over the Alvi & Settles[3] prediction of 45° without control (Fig. 17). The more acute the angle the weaker the leading shock will be, leading to a series of weaker shocks through the lambda foot, reducing wave drag.

https://doi.org/10.1017/S0001924000005042 Published online by Cambridge University Press

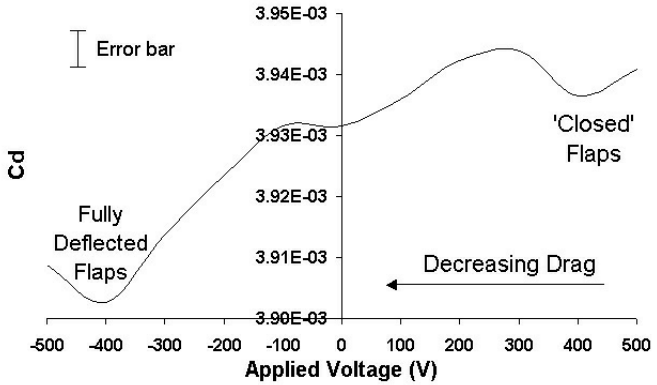


Figure 18. Drag coefficient *vs* applied voltage.

4.3 Drag coefficient

Losses in total pressure, P_0, correspond to a loss in momentum caused by drag. Although the isentropic assumption is valid for determining local Mach numbers throughout the test section, the total pressure loss is actually a result of the non-isentropic nature of the flow in the test section.

It may be seen that at each pressure tap the scanivalve measures a point drag (C_d'). By integrating over the test section, the total drag coefficient can be determined. Nagamatsu *et al*[10] presents the following formula for determining the point drag coefficient, C_d':

$$C_d' = 2\left[\frac{P_{0t}}{P_{01}}\right]^{(\gamma-1)} \cdot \left[\frac{P_t}{P_1}\right]^{\left(\frac{1}{\gamma}\right)} \cdot \left\{\frac{1-\left[\frac{P_t}{P_{0t}}\right]^{\frac{\gamma-1}{\gamma}}}{1-\left[\frac{P_1}{P_{01}}\right]^{\frac{1}{\gamma}}}\right\}^{(1/2)} \cdot \left\{1-\left[\frac{1-\left[\frac{P_1}{P_{0t}}\right]^{\frac{\gamma-1}{\gamma}}}{1-\left[\frac{P_1}{P_{01}}\right]^{\frac{1}{\gamma}}}\right]^{(1/2)}\right\} \quad . . (8)$$

From this relation, it can be calculated that the point drag is zero for all the pressure ports before the shock, as P_{0t} is equal to P_{01}, which makes the last term in Equation (8) have zero value. The point drag coefficients are integrated across the test section and the following integral is obtained:

$$C_d = \frac{1}{l}\int_{test\,section} C_d'\,\mathrm{d}x \quad . . (9)$$

Drag coefficients were calculated at various actuator deflections (Fig. 18). A positive voltage was applied to reduce deflection, whereas a negative voltage assisted deflection. It was not possible to reach the piezoceramic 1000V applied voltage limit due to arcing limitations observed above 500V.

A trend can be clearly observed from Fig. 18. As expected, a positive applied voltage, closing the flap, increases the drag coefficient and a negative voltage, assisting tip deflection, reduces the drag coefficient. A greater tip deflection will produce more mass transfer, improving the control effectiveness to a certain degree. The fluctuations on the above graph were the consequences of the inherent noise in the instrumentation.

This test section had a slot to actuator area of 1%. Chen[22] suggests that passive control using slots has an optimum porosity of 1 %, which should give a visible drag reduction. The increased coefficient at –500V could be due to excessive control, increasing coefficient as suggested by Chen. However, the error bar of the results is $\pm 5 \times 10^{-5}$ and that the increase is more likely due to system noise.

4.4 Actuator degradation

The actuators were tested electrically before and after wind tunnel testing in order that performance could be compared to check for any degradation. Moreover, if degradation did occur, then a qualitative amount could be determined. It was observed that the tip deflections due to the piezoelectric properties were similar before and after wind tunnel testing. If anything the magnitude of deflection increased, suggesting an instrument error, rather than a change in piezoelectric properties.

5.0 CONCLUSIONS

Experimental tests have shown that interaction control using piezoelectric actuators is feasible. Although a constant average pressure between the upstream (low pressure) and downstream (high pressure) was assumed, there is, in reality, a pressure gradient in the plenum chamber and spillage will occur around the edge of the actuators, where the flow escapes through the gaps between the model skin and the flap, thus reducing the pressure acting on the actuators. However, the magnitude of these effects is uncertain, though it appears small.

The use of FEM allows complex loads to be applied to theoretical models to optimise the unimorph design. A quadratic load is applied with a maximum pressure of 17·64kPa, which is equivalent to half the difference of the pressure rise over the shock. The pressure drops off to zero at the flap edges producing a more realistic loading that satisfies the boundary conditions.

The final unimorph design used a substrate thickness and Young's Modulus of 1·1mm and 70GPa, respectively. These values gives 0·5mm maximum tip deflection, which theoretically ensures closure and can be easily manufactured without defects.

The surface pressure distributions show local pressure maximum that indicates an extended leading shock followed by a local pressure minimum that is a result of boundary-layer thickening. In addition to a pressure plateau, these features indicate that the shock wave separates to form a lambda-like structure and therefore suggest a reduction in wave drag.

The pressure ratios before the plateau are reduced for increased voltage, reduced unimorph deflection, giving active control. Increased unimorph deflection leads to greater mass transfer from the higher pressure plenum chamber. This is reversed for downstream pressure ratios as increased mass transfer bleeds off the higher pressures to the lower pressures in the plenum chamber. It is assumed that with an applied 500V electric field to the piezoceramic that zero deflection of the unimorph results. Interaction characteristics are still observed for 500V due mainly to mass transfer that occurs through the surface slots and zero deflection is only an assumption, as precise deflection measurement devices are unavailable at present.

As expected, a positive applied voltage, closing the actuator flap, increases the drag coefficient, and a negative voltage, assisting tip deflection, reduces the drag coefficient. A greater tip deflection will produce more mass transfer, improving the control effectiveness to a certain degree. The fluctuations observed were the consequences of the inherent noise in the instrumentation.

REFERENCES

1. KOIDE, S., SAIDA, N. and OGATA, R. Correlation of separation angles induced by glancing interactions, *AIAA J*, 1996, **34**, (10), Technical Notes, pp 2198-2200.
2. GREEN, J.E. Interactions between shock waves and turbulent boundary-layers, *Prog Aerospace Sci*, 1969, **11**, pp 253-340.
3. ALVI, A. and SETTLES, G.S. Physical model of the swept shock wave boundary-layer interaction flow field, *AIAA J*, 1992, **30**, (9), pp. 2252-2258.

https://doi.org/10.1017/S0001924000005042 Published online by Cambridge University Press

4. INGER, G.R. Application of a shock-turbulent boundary-layer interaction theory in transonic flowfield analysis, AIAA Transonic Perspective Symposium, 1981, NASA/Ames Research Center, Moffett Field, California, USA.
5. KUBOTA, H. and STOLLERY, J.L. An experimental study of the interaction between a glancing shock wave and a turbulent boundary-layer, *J Fluid Mech*, 1982, **116**, pp.431-458.
6. ATKIN, C.J. and SQUIRE, L.C. A study of the interaction of a normal shock wave with a turbulent boundary-layer at Mach numbers between 1·30 and 1·55, *Eur J Mech, B/Fluids*, 1992, **11**, (1), pp 93-118.
7. SETTLES, G.S. and DOLLING, D.S. Swept shock-wave/boundary-layer interactions, *Prog Astro and Aero*, 1992, **141**, SEEBASS, A.R. (Ed), pp 505-574.
8. BAHI, L., ROSS, J.M., and NAGAMATSU, H.T., Passive shock wave/boundary-layer control for transonic airfoil drag reduction, 1983, AIAA 21st Aerospace Sciences meeting, 1983, Reno, USA.
9. SAVU, G. and TRIFU, O. Porous airfoils in transonic flow, *AIAA J*, 1984, **22**, (7) Technical Notes, pp 989-991.
10. NAGAMATSU, H.T., FICARRA, R.V. and DYER, R. Supercritical airfoil drag reduction by passive shock wave/boundary-layer control in the Mach number range ·75 to ·90, 1985, AIAA 23rd Aerospace Sciences meeting, 1985, Reno, Nevada, USA.
11. NAGAMATSU, H.T., MITTY, T.J. and NYBERG, G.A. Passive shock wave/boundary-layer control of a helicopter rotor airfoil in a contoured transonic wind tunnel, 1987, AIAA 25th Aerospace Sciences meeting, 1987, Reno, Nevada, USA.
12. RAGHUNATHAN, S. Effects of porosity strength on passive shock-wave/boundary-layer control, *AIAA J*, 1987, **25**, (5), pp 757-758.
13. RAGHUNATHAN, S., GRAY, J.L. and COOPER, R.K. Effects of inclination of holes on passive shock wave boundary-layer control, 1987, AIAA 25th Aerospace Sciences Meeting, 1987, Reno, Nevada, USA.
14. RAGHUNATHAN, S. and MABEY, D.G. Passive shock-wave/boundary-layer control on a wall-mounted model, *AIAA J*, 1987, **25**, (2), pp 275-278.
15. RAGHUNATHAN, S. Passive control of shock-boundary-layer interaction, *Prog Aerospace Sci*, 1988, **25**, pp 271-296.
16. BABINSKY, H. Control of swept shock wave/turbulent boundary-layer interactions, ISSW22, 1999, Imperial College, London, UK.
17. GIBSON, T.M., BABINSKY, H. and SQUIRE, L.C. Passive control of shock wave – boundary-layer interactions, *Aeronaut J*, **104**, (1033), 2000, pp 129-140.
18. COULDRICK, J.S. *et al* Swept shock wave boundary-layer interaction control with 'smart' flap actuators, Australian International Aerospace Conference, 2001, Canberra, Australia.
19. COULDRICK, J.S. *et al* Development of 'smart' flap actuators for swept shock wave boundary-layer interaction control, 2002, 40th AIAA Aerospace Sciences meeting and exhibition, 2002, Reno, USA.
20. COULDRICK, J.S. *et al* Design optimisation of 'smart' flap actuators for swept shock wave boundary-layer interaction control, 2002, Second Advances in Structural Engineering and Mechanics meeting, 2002, Pusan, Korea.
21. SQUIRE, L.C. Interaction of swept and unswept normal shock waves with boundary-layers, *AIAA J*, 1996, **34**, (10), pp 2099-2101.
22. CHEN, C. *et al*, Numerical study of porous airfoils in transonic flow, *AIAA J*, 1984, **22**, pp 989-991.

https://doi.org/10.1017/S0001924000005042 Published online by Cambridge University Press